Shape transition and fluctuations in neutron-rich Cr isotopes around $N = 40$

Koichi Sato,[1] Nobuo Hinohara,[1,2] Kenichi Yoshida,[3,4] Takashi Nakatsukasa,[1] Masayuki Matsuo,[3,4] and Kenichi Matsuyanagi[1,5]

[1]*RIKEN Nishina Center, Wako 351-0198, Japan*

[2]*Department of Physics and Astronomy, University of North Carolina, Chapel Hill, North Carolina 27599-3255, USA*

[3]*Graduate School of Science and Technology, Niigata University, Niigata 950-2181, Japan*

[4]*Department of Physics, Faculty of Science, Niigata University, Niigata 950-2181, Japan*

[5]*Yukawa Institute for Theoretical Physics, Kyoto University, Kyoto 606-8502, Japan*

The spherical-to-prolate shape transition in neutron-rich Cr isotopes from $N = 34$ to 42 is studied by solving the collective Schrödinger equation for the five-dimensional quadrupole collective Hamiltonian. The collective potential and inertial functions are microscopically derived with use of the constrained Hartree-Fock-Bogoliubov plus local quasiparticle random-phase approximation method. Nature of the quadrupole collectivity of low-lying states is discussed by evaluating excitation spectra and electric quadrupole moments and transition strengths. The result of calculation indicates that Cr isotopes around ^{64}Cr are prolately deformed but still possess transitional character; large-amplitude shape fluctuations dominate in their low-lying states.

I. INTRODUCTION

Recent experiments on neutron-rich Cr isotopes show that quadrupole collectivity appreciably develops toward ^{64}Cr with $N = 40$ [1–6]. Going from ^{58}Cr to ^{64}Cr, the excitation energy of the first excited 2^+_1 state decreases and $R_{4/2}$, the ratio of the excitation energy of the 4^+_1 state to that of the 2^+_1 state, increases. These data seem to indicate that a quantum phase transition from the spherical to deformed shapes takes place near $N = 40$. The microscopic origin of the enhanced quadrupole collectivity toward $N = 40$ has been actively discussed from various theoretical approaches: the Hartree-Fock-Bogoliubov (HFB) mean-field calculations using the Skyrme force [8] or the Gogny force [9], the spherical shell-model [7,10], and the projected deformed shell model [11]. These calculations have clarified the important role of the neutron $g_{9/2}$ and $d_{5/2}$ single-particle levels in the emergence of the quadrupole collectivity near $N = 40$. Although the spherical shell model calculations reproduce the experimental data rather well, the character of the quadrupole deformation, especially, the distinction between the equilibrium shape and shape fluctuations around it is not sufficiently clear.

In this paper, we investigate the nature of the quadrupole collectivity in low-lying states of the neutron-rich Cr isotopes $^{58-64}$Cr using an approach that treats the quadrupole deformations as dynamical variables. Thus, the distinction of the equilibrium shape and shape fluctuations is transparent. The deformation energy curve with respect to the axial quadrupole deformation was obtained in the Skyrme HFB mean-field calculation [8], which shows that the quadrupole instability occurs around $N = 38$–42. However, the deformed minima are extremely shallow in these nuclei, suggesting a transitional character. In such transitional situations, one naturally expects that large-amplitude shape fluctuations play an important role in determining the properties of low-lying excited states. Therefore, we take the five-dimensional (5D) quadrupole collective Hamiltonian approach [12], which is

capable of describing the large-amplitude quadrupole shape fluctuations associated with the quantum shape transition. It enables us to treat a variety of quadrupole deformation phenomena (vibrational, spherical-prolate transitional, rotational, γ-unstable, triaxial, oblate-prolate shape-coexistent situations, etc.) on an equal footing. Dynamical variables of the 5D quadrupole collective Hamiltonian approach are the magnitude and triaxiality of quadrupole deformation (β, γ) and the three Euler angles. The 5D collective Hamiltonian is characterized by seven functions: the collective potential, three vibrational inertial functions (also called vibrational masses), and three rotational inertial functions. To evaluate the inertial functions, the Inglis-Belyaev (IB) cranking formula has been conventionally used. However, it is well known that the contribution of the time-odd components of the moving mean field is ignored in the IB cranking formula, which leads to the overestimation of excitation energies [14,15].

The constrained Hartree-Fock-Bogoliubov plus local quasiparticle random-phase approximation (CHFB + LQRPA) method [16] is a method which can overcome the shortcoming of the IB cranking formula. This method has been successfully applied to several phenomena: shape coexistence/fluctuation in Se and Kr isotopes [14,16,19], development of triaxial deformation in ^{110}Mo [20], and shape fluctuations in neutron-rich Mg isotopes [21]. Use of the Skyrme energy density functional in solving the CHFB + LQRPA equations has also been initiated for the axially symmetric quadrupole Hamiltonian [22]. In this paper, we solve the LQRPA equations with use of the pairing-plus-quadrupole (P + Q) model [12] including the quadrupole pairing interaction. For the collective Hamiltonian quantized according to the Pauli prescription, we solve the collective Schrödinger equation to obtain the excitation energies, vibrational wave functions, $E2$-transition strengths, and moments.

This paper is organized as follows. We recapitulate the theoretical framework in Sec. II. In Sec. III, we present

results of calculation for $^{58-66}$Cr and discuss the nature of quadrupole collectivity in their low-lying states. We then discuss similarities and differences of the quadrupole shape transition near ^{64}Cr with $N=40$ and that near ^{32}Mg with $N=20$. Conclusions are given in Sec. IV.

II. THEORETICAL FRAMEWORK

In this section, we briefly summarize the framework of our collective Hamiltonian approach. See Ref. [16] for details.

A. 5D quadrupole collective Hamiltonian

The 5D quadrupole collective Hamiltonian is given by

$$\mathcal{H}_{\text{coll}} = T_{\text{vib}} + T_{\text{rot}} + V(\beta, \gamma), \tag{1}$$

$$T_{\text{vib}} = \frac{1}{2}D_{\beta\beta}(\beta,\gamma)\dot{\beta}^2 + D_{\beta\gamma}(\beta,\gamma)\dot{\beta}\dot{\gamma} + \frac{1}{2}D_{\gamma\gamma}(\beta,\gamma)\dot{\gamma}^2, \tag{2}$$

$$T_{\text{rot}} = \frac{1}{2}\sum_{k=1}^{3}\mathcal{J}_k(\beta,\gamma)\omega_k^2, \tag{3}$$

where T_{vib} and T_{rot} represent the vibrational and rotational kinetic energies, while V the collective potential energy. The velocities of the vibrational motion are described in terms of the time derivatives $(\dot{\beta},\dot{\gamma})$ of the quadrupole deformation variables (β,γ) representing the magnitude and the triaxiality of the quadrupole deformation, respectively. The three components ω_k of the rotational angular velocity are defined with respect to the principal axes associated with the rotating nucleus. The moments of inertia are parametrized as $\mathcal{J}_k(\beta,\gamma) = 4\beta^2 D_k(\beta,\gamma)\sin^2\gamma_k$ with $\gamma_k = \gamma - 2\pi k/3$. The inertial functions for vibration (vibrational masses) $D_{\beta\beta}$, $D_{\beta\gamma}$ and $D_{\gamma\gamma}$, and those for rotation (rotational masses) D_k are functions of β and γ.

The collective potential and inertial functions are determined with the CHFB + LQRPA method as explained in the next subsection. Once they are determined as functions of (β,γ), we quantize the collective Hamiltonian according to the Pauli prescription. The collective Schrödinger equation for the quantized collective Hamiltonian is given by

$$\{\hat{T}_{\text{vib}} + \hat{T}_{\text{rot}} + V\}\Psi_{\alpha IM}(\beta,\gamma,\Omega) = E_{\alpha I}\Psi_{\alpha IM}(\beta,\gamma,\Omega), \tag{4}$$

where

$$\hat{T}_{\text{vib}} = \frac{-1}{2\sqrt{WR}}\left\{\frac{1}{\beta^4}\left[\left(\partial_\beta \beta^2 \sqrt{\frac{R}{W}}D_{\gamma\gamma}\partial_\beta\right)\right.\right.$$
$$\left.\left. - \partial_\beta\left(\beta^2\sqrt{\frac{R}{W}}D_{\beta\gamma}\partial_\gamma\right)\right]\right.$$
$$+ \frac{1}{\beta^2\sin 3\gamma}\left[-\partial_\gamma\left(\sqrt{\frac{R}{W}}\sin 3\gamma D_{\beta\gamma}\partial_\beta\right)\right.$$
$$\left.\left. + \partial_\gamma\left(\sqrt{\frac{R}{W}}\sin 3\gamma D_{\beta\beta}\partial_\gamma\right)\right]\right\} \tag{5}$$

and

$$\hat{T}_{\text{rot}} = \sum_k \frac{\hat{I}_k^2}{2\mathcal{J}_k}. \tag{6}$$

Here, $R(\beta,\gamma)$ and $W(\beta,\gamma)$ are defined as

$$R(\beta,\gamma) = D_1(\beta,\gamma)D_2(\beta,\gamma)D_3(\beta,\gamma), \tag{7}$$

$$W(\beta,\gamma) = \{D_{\beta\beta}(\beta,\gamma)D_{\gamma\gamma}(\beta,\gamma) - [D_{\beta\gamma}(\beta,\gamma)]^2\}\beta^{-2}. \tag{8}$$

The collective wave function $\Psi_{\alpha IM}(\beta,\gamma,\Omega)$ is specified by the total angular momentum I, its projection onto the z axis of the laboratory frame M, and α distinguishing the states with the same I and M. It can be written as a sum of products of the vibrational and rotational wave functions:

$$\Psi_{\alpha IM}(\beta,\gamma,\Omega) = \sum_{K=\text{even}} \Phi_{\alpha IK}(\beta,\gamma)\langle\Omega|IMK\rangle, \tag{9}$$

where

$$\langle\Omega|IMK\rangle = \sqrt{\frac{2I+1}{16\pi^2(1+\delta_{K0})}}\left[\mathcal{D}_{MK}^I(\Omega) + (-)^I\mathcal{D}_{M-K}^I(\Omega)\right]. \tag{10}$$

$\mathcal{D}_{MK}^I$ is the Wigner rotation matrix and K is the projection of the angular momentum onto the z axis in the body-fixed frame. The summation over K is taken from 0 to I for even I and from 2 to $I-1$ for odd I.

The vibrational wave functions in the body-fixed frame, $\Phi_{\alpha IK}(\beta,\gamma)$, are normalized as

$$\int d\beta d\gamma |\Phi_{\alpha I}(\beta,\gamma)|^2 |G(\beta,\gamma)|^{\frac{1}{2}} = 1, \tag{11}$$

where

$$|\Phi_{\alpha I}(\beta,\gamma)|^2 \equiv \sum_{K=\text{even}} |\Phi_{\alpha IK}(\beta,\gamma)|^2, \tag{12}$$

and the volume element $|G(\beta,\gamma)|$ is given by

$$|G(\beta,\gamma)| = 4\beta^8 W(\beta,\gamma)R(\beta,\gamma)\sin^2 3\gamma. \tag{13}$$

The symmetries and boundary conditions of the collective Hamiltonian and wave functions are discussed in Ref. [23].

B. The CHFB + LQRPA method

We determine the collective potential and inertial functions with the CHFB + LQRPA method. It is derived on the basis of the adiabatic self-consistent collective coordinate (ASCC) method [15,17,18] by assuming that there is a one-to-one mapping from a point on the collective submanifold embedded in the large-dimensional time-dependent HFB phase space to a point in the (β,γ) deformation space. In the CHFB + LQRPA method, the inertial functions are derived by transforming the local canonical coordinates determined by the LQRPA normal modes to the (β,γ) degrees of freedom.

We first solve the CHFB equation

$$\delta\langle\phi(\beta,\gamma)|\hat{H}_{\text{CHFB}}(\beta,\gamma)|\phi(\beta,\gamma)\rangle = 0, \tag{14}$$

$$\hat{H}_{\text{CHFB}} = \hat{H} - \sum_\tau \lambda^{(\tau)}\hat{N}^{(\tau)} - \sum_m \mu^{(m)}\hat{D}_{2m}^{(+)} \tag{15}$$

with the constraints on the particle numbers and quadrupole deformation parameters:

$$\langle\phi(\beta,\gamma)|\hat{N}^{(\tau)}|\phi(\beta,\gamma)\rangle = N_0^{(\tau)}, \quad (\tau = n, p), \quad (16)$$

$$\langle\phi(\beta,\gamma)|\hat{D}_{2m}^{(+)}|\phi(\beta,\gamma)\rangle = D_{2m}^{(+)}, \quad (m = 0, 2). \quad (17)$$

Here, $\hat{D}_{2m}^{(+)}$ denotes Hermitian quadrupole operators, $\hat{D}_{20}$ and $(\hat{D}_{22} + \hat{D}_{2-2})/2$ for $m = 0$ and 2, respectively. We define the quadrupole deformation variables (β,γ) in terms of the expectation values of the quadrupole operators

$$\beta\cos\gamma = \eta D_{20}^{(+)} = \eta\langle\phi(\beta,\gamma)|\hat{D}_{20}^{(+)}|\phi(\beta,\gamma)\rangle, \quad (18)$$

$$\frac{1}{\sqrt{2}}\beta\sin\gamma = \eta D_{22}^{(+)} = \eta\langle\phi(\beta,\gamma)|\hat{D}_{22}^{(+)}|\phi(\beta,\gamma)\rangle, \quad (19)$$

where η is a scaling factor (see Ref. [16] for the explicit expression). Then, we solve the LQRPA equations for vibration on top of the CHFB states obtained above,

$$\delta\langle\phi(\beta,\gamma)|[\hat{H}_{\text{CHFB}}(\beta,\gamma), \hat{Q}^i(\beta,\gamma)]$$
$$-\frac{1}{i}\hat{P}_i(\beta,\gamma)|\phi(\beta,\gamma)\rangle = 0, \quad (20)$$

$$\delta\langle\phi(\beta,\gamma)|\left[\hat{H}_{\text{CHFB}}(\beta,\gamma), \frac{1}{i}\hat{P}_i(\beta,\gamma)\right]$$
$$-C_i(\beta,\gamma)\hat{Q}^i(\beta,\gamma)|\phi(\beta,\gamma)\rangle = 0, \quad (i = 1, 2). \quad (21)$$

The infinitesimal generators, $\hat{Q}^i(\beta,\gamma)$ and $\hat{P}_i(\beta,\gamma)$, are locally defined at every point of the (β,γ) deformation space. The quantity $C_i(\beta,\gamma)$ is related to the eigenfrequency $\omega_i(\beta,\gamma)$ of the local normal mode through $\omega_i^2(\beta,\gamma) = C_i(\beta,\gamma)$. It is worth noting that these equations are valid also for regions with negative curvature ($C_i(\beta,\gamma) < 0$) where $\omega_i(\beta,\gamma)$ takes an imaginary value.

The rotational moments of inertia are calculated by solving the LQRPA equation for rotation on each CHFB state. It is an extension of the Thouless-Valatin equation [24] for the HFB equilibrium state to non-equilibrium CHFB states. We call the moments of inertia $\mathcal{J}_k(\beta,\gamma)$ thus determined 'LQRPA moments of inertia.'

We solve the collective Schrödinger equation (4) to obtain excitation energies and vibrational wave functions. Then, electric transition strengths and moments are readily calculated (see Ref. [19] for details).

C. Details of the numerical calculation

The CHFB + LQRPA method can be used in conjunction with any effective interaction (e.g., density-dependent effective interaction such as Skyrme functionals, or other modern nuclear density functionals). In fact, the use of the Skyrme functional for the LQRPA approach has been initiated for axially symmetric quadrupole Hamiltonian [22]. In this study, however, we adopt a version of the pairing-plus-quadrupole (P + Q) model [12] including the quadrupole pairing interaction as well as the monopole pairing interaction for computational simplicity. We take two harmonic-oscillator shells with $N_{sh} = 3, 4$ and $N_{sh} = 2, 3$ for neutrons and protons,

respectively. The single-particle energies are determined with the constrained Skyrme-HFB calculations at the spherical shape using the HFBTHO code [25]. The single-particle energies in the canonical basis obtained in the Skyrme-HFB calculations are then scaled with the effective mass of the SkM* functional $m^*/m = 0.79$ for the use of the P + Q model, because it is designed to be used for single particles whose mass is the bare nucleon mass. In these Skyrme-HFB calculations, we employ the SkM* functional and the volume-type pairing with the pairing strength $V_0 = -180$ MeV fm^{-3}. The pairing strength has been adjusted such that the calculated neutron pairing gaps at the HFB minima reproduce the experimental gaps in $^{58-64}$Cr determined from the odd-even mass differences [26].

To determine the quadrupole pairing strengths in the P + Q model, we follow the Sakamoto-Kishimoto prescription [27] to restore the local Galilean invariance broken by the monopole pairing. With this prescription, once we set the values of the monopole pairing strengths $G_0^{(\tau)}(\tau = n, p)$, the quadrupole pairing strengths are self-consistently determined from them at the spherical shape. The other parameters of the P + Q model are determined in the following way. For ^{62}Cr (situated in the middle of the isotopic chain), the monopole pairing strengths and quadrupole particle-hole interaction strength χ are adjusted to approximately reproduce the HFB equilibrium deformation and the pairing gaps at the spherical and HFB equilibrium shapes. For the other nuclei ^{58,60,64,66}Cr, we assume the simple mass number dependence according to Baranger and Kumar [12]: $G_0^{(\tau)} \sim A^{-1}$ and $\chi' \equiv \chi b^4 \sim A^{-5/3}$ (b denotes the oscillator-length parameter). We omit the Fock term as in the conventional treatment of the P + Q model.

The CHFB + LQRPA equations are solved at 60×60 mesh points in the (β,γ) plane defined by

$$\beta_i = (i - 0.5) \times 0.01, \quad (i = 1, \ldots, 60), \quad (22)$$

$$\gamma_j = (j - 0.5) \times 1°, \quad (j = 1, \ldots, 60). \quad (23)$$

For the calculation of the $E2$ transitions and moments, we use the standard values of effective charges $(e_{\text{eff}}^{(n)}, e_{\text{eff}}^{(p)}) = (0.5, 1.5)$.

III. RESULTS AND DISCUSSION

In this section, we present the numerical results for $^{58-66}$Cr and discuss the nature of quadrupole collectivity in their low-lying states. We furthermore discuss the similarities and differences with Mg isotopes around $N = 20$.

A. Collective potentials and inertial functions

We plot the collective potential $V(\beta,\gamma)$ calculated for $^{58-66}$Cr in Fig. 1. The location of the absolute minimum is indicated by the (blue) circle. In ^{58}Cr, the absolute minimum is located at a nearly spherical shape. Although the minimum shifts to larger deformation in ^{60}Cr, the collective potential is extremely soft in the β direction. A more pronounced local minimum appears at larger deformation in ^{62}Cr, and the minimum becomes even deeper in ^{64}Cr. In ^{66}Cr, the collective
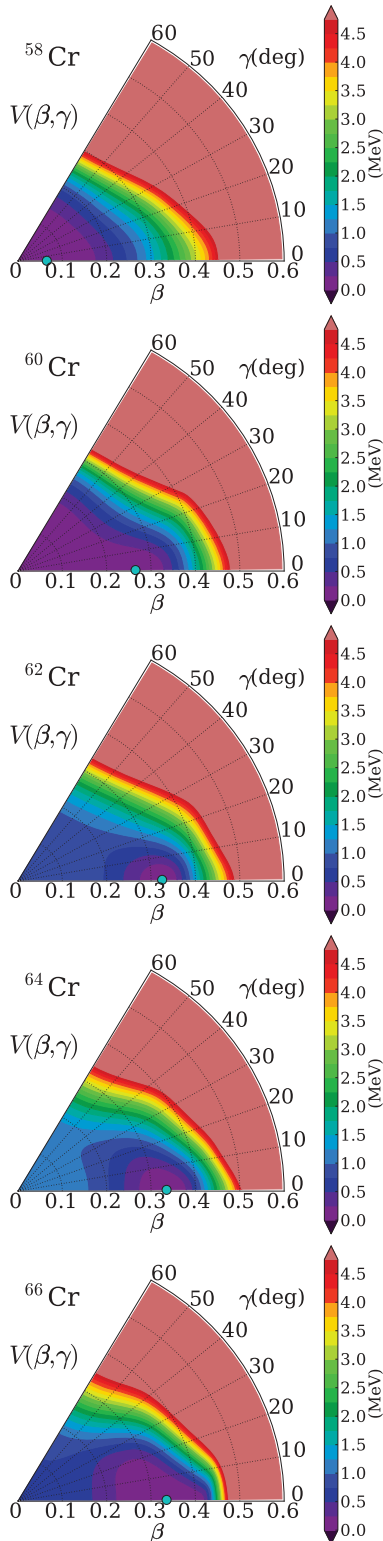
FIG. 1. (Color online) Collective potential energy surfaces $V(\beta, \gamma)$ for $^{58-66}$Cr. The regions higher than 5 MeV (measured from the HFB minima) are colored rosy-brown.
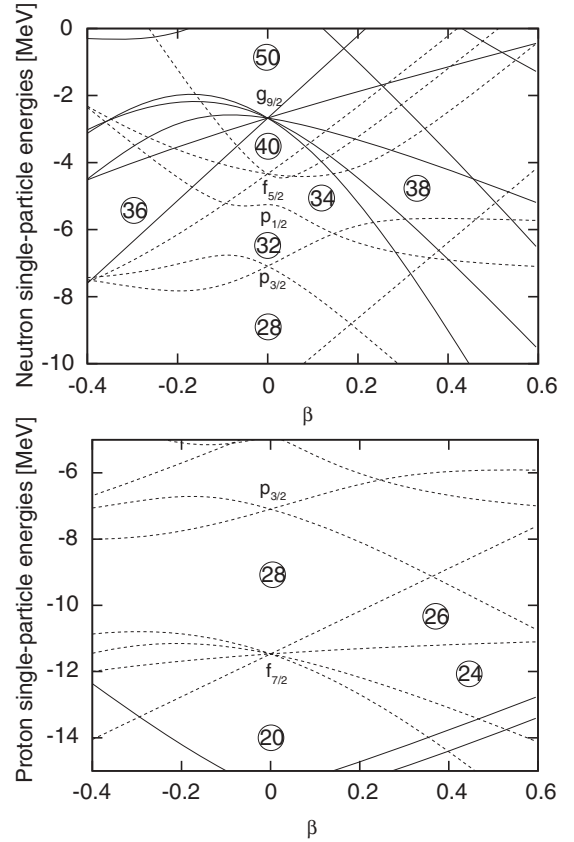

FIG. 2. Nilsson diagrams for neutrons (upper) and protons (lower) in ^{62}Cr as functions of β, calculated as in Ref. [13]. The levels with the positive (negative) parity are plotted with solid (dotted) lines.

isotopic chain toward $N = 40$. In Fig. 2, we plot the Nilsson diagrams of neutrons and protons as functions of β calculated for ^{62}Cr as in Ref. [13]. This is similar to Figs. 5(a) and 5(b) in Ref. [8]. In ^{58}Cr, the neutron and proton shell effects for $N = 34$ and $Z = 24$ are in competition. The appearance of the potential minimum in the slightly deformed region in Fig. 1 suggests that the neutron shell effects dominate over the proton ones. On the other hand, in ^{62}Cr, the deformed shell effects for $N = 38$ and $Z = 24$ are in cooperation and lead to the prolate potential minimum.

In Fig. 3, we plot the neutron and proton monopole pairing gaps $\Delta_0^{(n)}(\beta, \gamma)$ and $\Delta_0^{(p)}(\beta, \gamma)$, the vibrational inertial function $D_{\beta\beta}(\beta, \gamma)$, and the rotational moment of inertia $\mathcal{J}_1(\beta, \gamma)$, calculated for ^{62}Cr. Figure 3(c) clearly shows that the vibrational inertial function is well correlated with the magnitudes of the pairing gaps: $D_{\beta\beta}(\beta, \gamma)$ becomes small in the spherical region where $\Delta_0^{(n)}$ and $\Delta_0^{(p)}$ take large values. One might be concerned for complicated behaviors of $D_{\beta\beta}(\beta, \gamma)$ in the strongly deformed region. However, they hardly affect low-lying states, because the collective potential energy is very high there and contributions from this region to the vibrational wave functions are negligibly small. Figure 3(d) clearly indicates that the rotational moment of inertia also has a strong correlation with the pairing gaps. It takes the maximum value in the prolate region around $\beta \simeq 0.35$. Both the neutron and proton pairing gaps become small there due
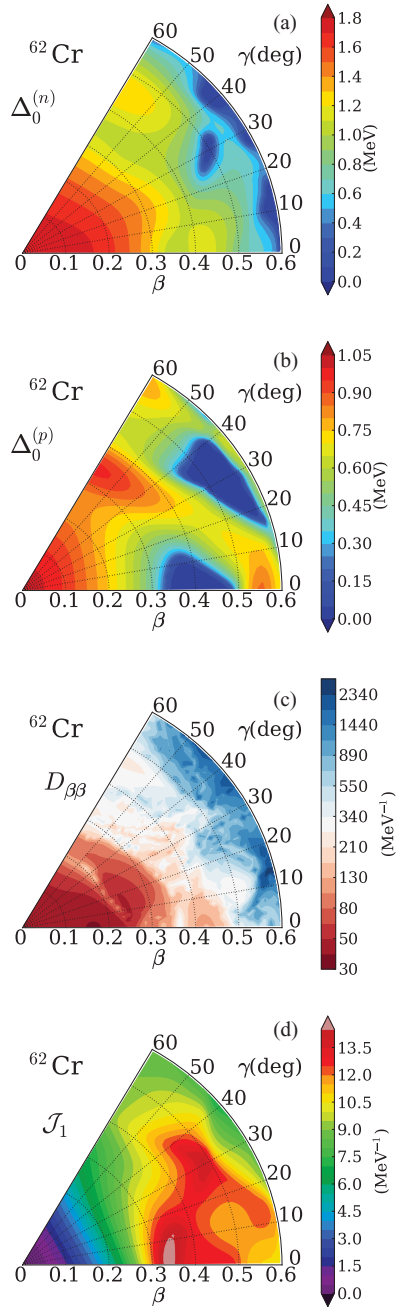
potential becomes slightly softer than in ^{64}Cr. These potential energy surfaces indicate that a quantum shape transition from a spherical to a prolately deformed shape takes place along the

FIG. 3. (Color online) (a) Neutron monopole pairing gap $\Delta_0^{(n)}(\beta, \gamma)$, calculated for ^{62}Cr. (b) Proton monopole pairing gap $\Delta_0^{(p)}(\beta, \gamma)$. (c) Vibrational inertial function $D_{\beta\beta}(\beta, \gamma)$. (d) Rotational moment of inertia $\mathcal{J}_1(\beta, \gamma)$.

to the deformed shell gaps for $N = 38$ and $Z = 24$, see Fig. 2. In particular, the proton pairing gap almost vanishes. It results in the increase of the moment of inertia. As we shall see later, this enhancement promotes the localization of the vibrational wave functions in the (β, γ) plane for excited states with nonzero angular momenta. The rotational and vibrational inertial functions for the other isotopes are qualitatively the same as those for ^{62}Cr. The enhancement of the moments of inertia mentioned above grows gradually with increasing neutron number up to $N = 40$.
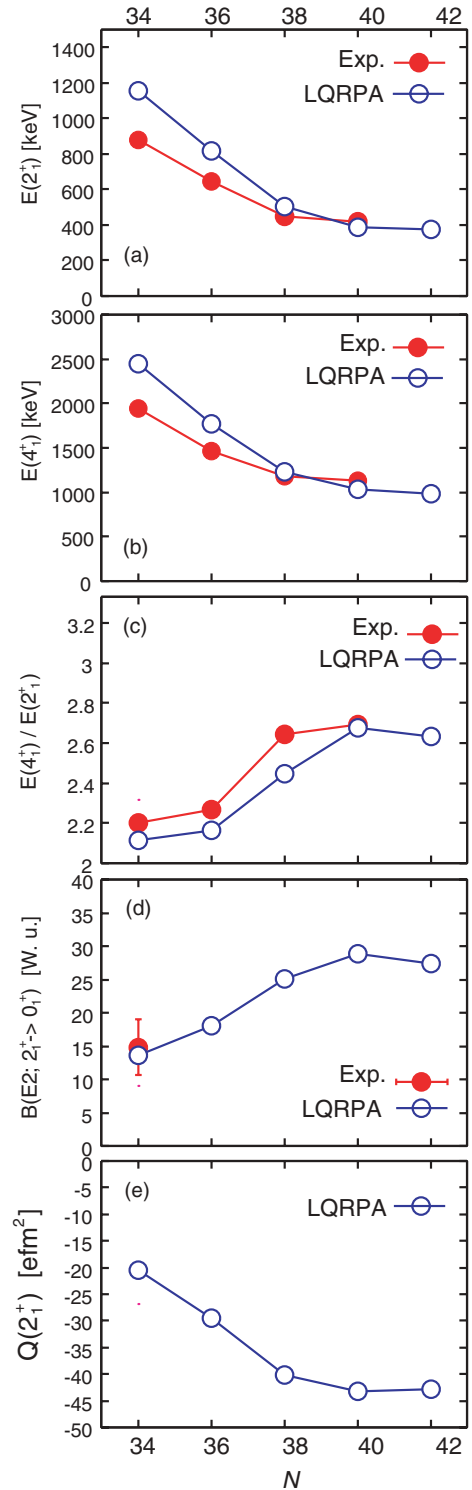

FIG. 4. (Color online) (a) Excitation energies of the 2_1^+ states for $^{58-66}$Cr. (b) Excitation energies of the 4_1^+ states. (c) Ratios of $E(4_1^+)$ to $E(2_1^+)$. (d) Reduced $E2$ transition probabilities $B(E2; 2_1^+ \rightarrow 0_1^+)$ in Weisskopf units. (e) Spectroscopic quadrupole moments of the 2_1^+ states. Experimental data are taken from Refs. [2,3,5,6].

B. Yrast states in $^{58-66}$Cr

We show in Fig. 4 the excitation energies of the 2_1^+ and 4_1^+ states, their ratios $R_{4/2}$, the $E2$ transition strengths

TABLE I. Excitation energies of the 2_1^+ state $E(2_1^+)$ in keV, the ratios $R_{4/2}$ of $E(4_1^+)$ to $E(2_1^+)$, and $B(E2;2_1^+ \rightarrow 0_1^+)$ in Weisskopf units for ^{64}Cr and ^{66}Fe. Experimental data are taken from Refs. [6,28].

	Calc.			Exp.		
	$E(2_1^+)$	$R_{4/2}$	$B(E2)$	$E(2_1^+)$	$R_{4/2}$	$B(E2)$
^{64}Cr	386	2.68	28.8	420	2.69	
^{66}Fe	685	2.29	15.5	573	2.47	21.0

$B(E2;2_1^+ \rightarrow 0_1^+)$, and the spectroscopic quadrupole moments of the 2_1^+ states, together with the available experimental data. The decrease in the excitation energies of the 2_1^+ and 4_1^+ states toward $N = 40$ and the increase in their ratio from $N = 36$ to $N = 40$ are well described and indicate that the nature of the quadrupole collectivity gradually changes from vibrational to rotational as the neutron number increases. However, the ratio $R_{4/2}$ at $N = 40$ is still 2.68, which is considerably smaller than the rigid-rotor value 3.33. The $B(E2)$ values and spectroscopic quadrupole moments $Q(2_1^+)$ also suggest the onset of deformation: $B(E2)$ increases and the magnitude of the spectroscopic quadrupole moments, which has a negative sign indicating a prolate shape, increase with increasing neutron number and both of them reach a maximum at $N = 40$.

In Table I, we compare the results for ^{64}Cr with those for ^{66}Fe. (In the calculation for ^{66}Fe, the single-particle energies and the P + Q parameters are determined following the same procedure as explained in Sec. II C. In particular, the latter are exactly the same as those for ^{66}Cr.) Experimental data indicate that the quadrupole collectivity is stronger in ^{64}Cr than in

^{66}Fe: the smaller $E(2_1^+)$ and the larger $R_{4/2}$ and $B(E2)$ values for ^{64}Cr than those for ^{66}Fe. Our calculation reproduces these features quite well.

We depict in Figs. 5 and 6 the squared vibrational wave functions multiplied by β^4 for the 0_1^+, 2_1^+ and 4_1^+ states in $^{58-66}$Cr and those without the β^4 factor for the 0_1^+ and 2_1^+ states in ^{60}Cr and ^{64}Cr, respectively. The β^4 factor comes from the volume element and carries its dominant β dependence [see Eqs. (11) and (13)]. The wave functions look quite different between the two cases. For instance, while the nonweighted 0_1^+ wave function for ^{60}Cr shown in Fig. 6 distributes around the spherical shape, the β^4 factor changes it to the arcuate pattern seen in Fig. 5. In ^{58}Cr and ^{60}Cr, the β^4-weighted 0_1^+ wave functions exhibit arcuate distributions around $\beta = 0.2$ covering the entire γ region. Closely looking, one finds that, while the distribution for ^{58}Cr is almost uniform in the γ direction, it is slightly leaning to the prolate side for ^{60}Cr.

With increasing neutron number, the 0_1^+ wave function localizes more and more on the prolate side, reflecting the deepening of the prolate minima (see the collective potential in Fig. 1). In ^{62}Cr, the 0_1^+ wave function still spreads over the entire γ region, although it has a clear concentration on the prolate side. In ^{64}Cr, one can see a distinct peak around the prolate potential minimum, and the 0_1^+ wave function is most localized at ^{64}Cr. The vibrational wave functions clearly indicate the shape transition from spherical to prolate along the isotopic chain.

For all these isotopes, one can see that the prolate peak grows with increasing angular momentum. This is due to the enhancement of the moments of inertia on the prolate side we have already seen in Fig. 3. Even in ^{58}Cr whose ground state is rather spherical, the 2_1^+ and 4_1^+ states are weakly localized
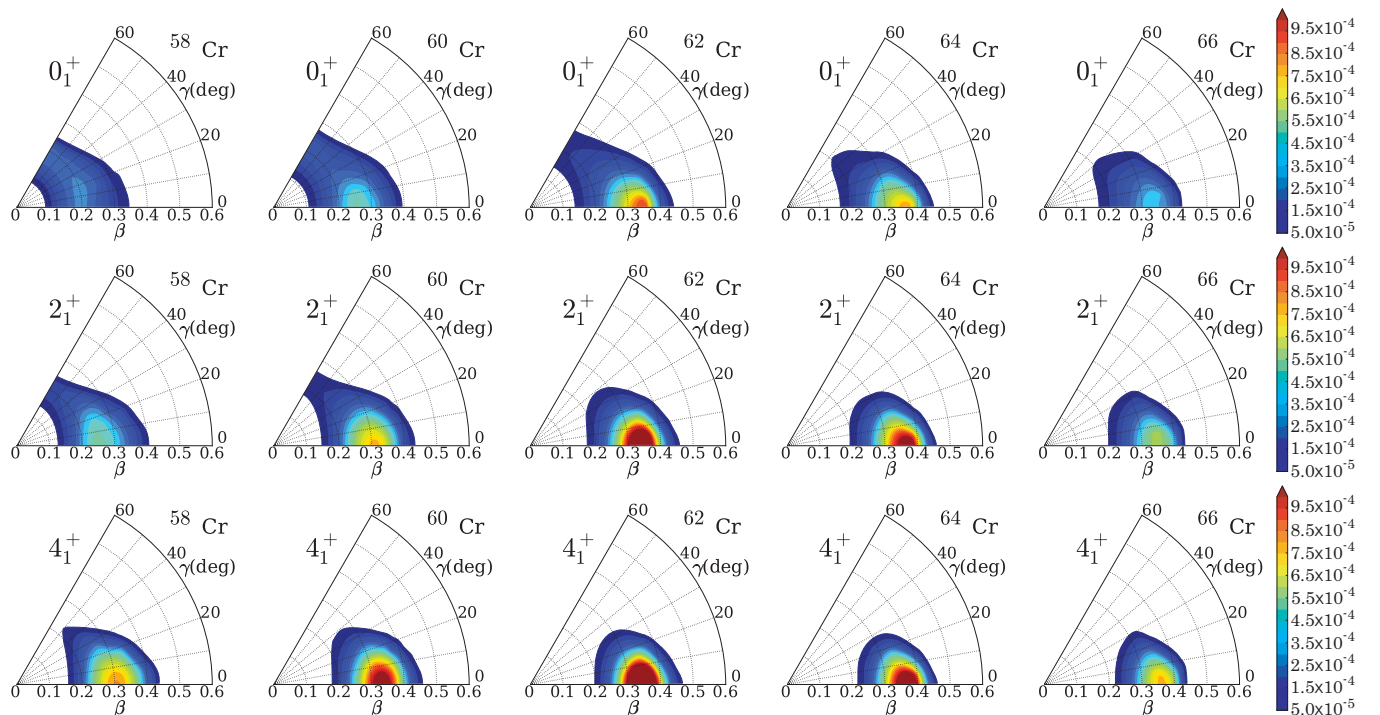

FIG. 5. (Color online) Squared vibrational wave functions multiplied by β^4, $\beta^4 \sum_K |\Psi_{\alpha IK}(\beta,\gamma)|^2$, for the 0_1^+, 2_1^+, and 4_1^+ states in $^{58-66}$Cr.
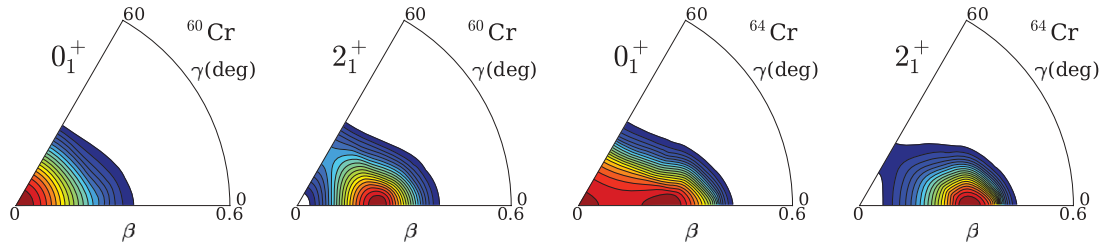
FIG. 6. (Color online) Vibrational wave function squared, $\sum_K |\Psi_{\alpha I K}(\beta, \gamma)|^2$, for the 0_1^+ and 2_1^+ states in ^{60}Cr and ^{64}Cr. The contour lines are drawn at every twentieth part of the maximum value.

on the prolate side, which results in the finite spectroscopic quadrupole moment shown in Fig. 4. In ^{64}Cr, the 2_1^+ and 4_1^+ wave functions are well localized on the prolate side, although the ground state wave function still exhibits non-negligible shape fluctuation in the γ direction. Due to the growth of localization of the wave functions, higher angular momentum states acquire more rotor-like character than the ground state. This fact can be quantified by calculating the ratio

$$R_{6/4/2} \equiv (E(6_1^+) - E(2_1^+))/(E(4_1^+) - E(2_1^+)). \quad (24)$$

For instance, $R_{6/4/2} = 2.42$ for ^{64}Cr, which is fairly close to the rigid-rotor value 2.57, although the calculated $R_{4/2}$ is 2.67 which is far from the rigid-rotor value 3.33. These results clearly indicate the importance of dynamical effects of rotation on the nuclear shape.

Lenzi *et al.* [7] evaluated the intrinsic quadrupole moments $Q_{\text{int}}(I)$ for the yrast states of $^{62-66}$Cr using the spectroscopic quadrupole moments $Q(I)$ obtained in their shell-model calculation and the well-known relation between them for the axially symmetric deformation with $K = 0$. The resulting $Q_{\text{int}}(I)$ stay approximately constant along the yrast sequences in ^{62,64,66}Cr, and they interpreted this as a fingerprint of a rigid rotor behavior. We have evaluated $Q_{\text{int}}(I)$ in the same way as Lenzi *et al.* but using our calculated $Q(I)$. The resulting $Q_{\text{int}}(I)$ values are similar to those of Lenzi *et al.* We feel, however, that this fact is insufficient to conclude that $^{62-66}$Cr are good rotors because $Q(I)$ are average values that are

insensitive to the shape fluctuations. We need to examine the properties of nonyrast states which are sensitive to shape fluctuation effects. We also note that $Q(I)$ does not carry direct information about the ground state, and that, according to our calculation, the ground-state vibrational wave function is significantly different from those of the other yrast states with $I \neq 0$.

C. Nonyrast states in $^{58-66}$Cr

To understand the nature of quadrupole collectivity, it is important to examine the properties of the excited bands including their interband transitions to the ground band, although they have not been observed experimentally yet. As typical examples of the calculated results, we display in Figs. 7 and 8 the excitation spectra and the $B(E2)$ values of the low-lying states in ^{60}Cr and ^{64}Cr. (The low-lying states of ^{58}Cr and ^{66}Cr have qualitatively the same features as those of ^{60}Cr and ^{64}Cr, respectively. Those of ^{62}Cr have an intermediate character between ^{60}Cr and ^{64}Cr.)

Let us first discuss the ^{60}Cr case. We notice that the calculated excitation spectrum exhibits some features characteristic of the 5D harmonic oscillator (HO) limit: approximately equal level spacing in the ground band, approximate degeneracy of the 4_1^+ and 2_2^+ states, nearly equal values of $B(E2; 0_2^+ \to 2_1^+)$ and $B(E2; 4_1^+ \to 2_1^+)$, which are about twice of $B(E2; 2_1^+ \to 0_1^+)$, etc. On the other hand, we also notice significant
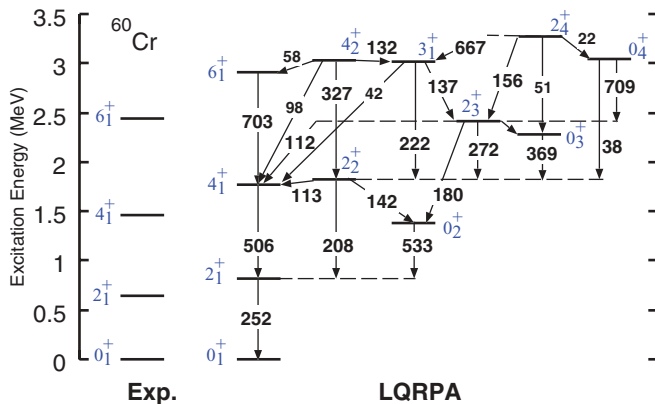

FIG. 7. (Color online) Excitation energies and $B(E2)$ values for ^{60}Cr in comparison with experimental data. Values on arrows indicate $B(E2)$ in units of e^2fm^4. Only $B(E2)$ values larger than 1 Weisskopf unit are shown. Experimental data are taken from Ref. [3].
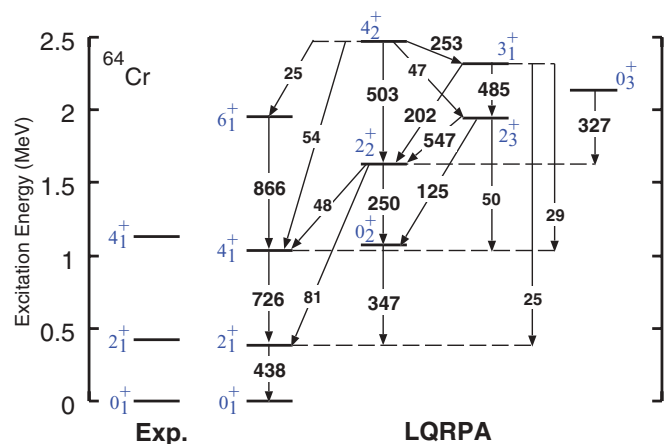

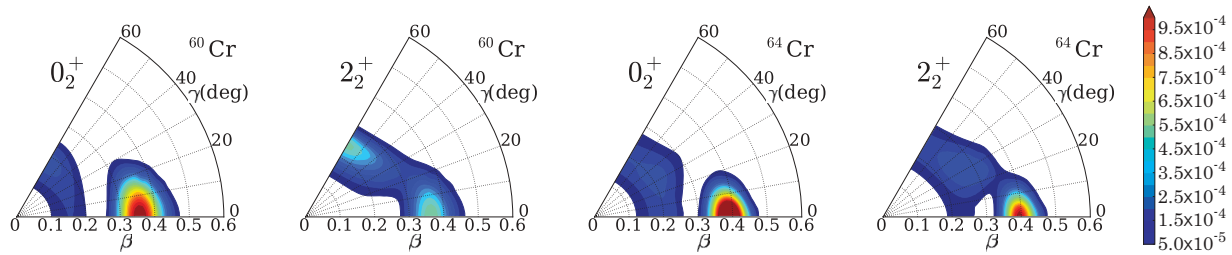FIG. 8. (Color online) Same as Fig. 7 but for ^{64}Cr. The experimental data are taken from Ref. [6].

FIG. 9. (Color online) Squared vibrational wave functions multiplied by β^4, $\beta^4 \sum_K |\Psi_{\alpha I K}(\beta, \gamma)|^2$, for the 0_2^+ and 2_2^+ states in ^{60}Cr and ^{64}Cr.

deviations from that limit. First, the 0_2^+ state is considerably lower than the 4_1^+ and 2_2^+ states. Second, the $E2$ transitions forbidden in the HO limit are sizable; e.g., those from the 2_2^+ state to the 4_1^+ and 0_2^+ states are fairly large. Third, the $B(E2)$ value from the 2_2^+ state to the 2_1^+ state is less than half of those from the 4_1^+ and 0_2^+ states.

To examine these anharmonicities, let us look into the vibrational wave functions of the excited states. The β^4-weighted and nonweighted vibrational wave functions of the 0_2^+ and 2_2^+ states are displayed in Figs. 9 and 10, respectively. The 0_2^+ wave function exhibits two components: one around the spherical shape and the other around $\beta = 0.35$. Although it has a β-vibrational feature, i.e., a node in the β direction, it also exhibits a considerable deviation from the 5D HO limit, in which the deformed component concentrating on the prolate side would spread uniformly over the γ direction. We can see a deviation from the 5D HO limit also in the 2_2^+ state. The β^4-weighted 2_2^+ wave function spreads from the prolate to the oblate sides. However, the nonweighted wave function reveals that it also has the β-vibrational component. In fact, this state is a superposition of the large-amplitude γ-vibrational component spreading over the entire γ region and the β-vibrational component. In the 5D HO limit, the 2_3^+ wave function has a node in the β direction, while the 2_2^+ wave function has no node. The calculated 2_2^+ wave functions indicate significant mixing of these components.

Let us proceed to the ^{64}Cr case. We immediately notice some features different from ^{60}Cr. First, the approximate degeneracy of the 4_1^+ and 2_2^+ states seen in ^{60}Cr is completely lifted here. Second, the $E2$ transitions within the ground band are much stronger than those in ^{60}Cr. Third, two low-lying excited bands appear: one consisting of the $0_2^+, 2_2^+$ and 4_2^+ states (excited band I), and the other consisting of the $2_3^+, 3_1^+,$ 4_3^+ states (excited band II, the 4_3^+ state not shown here is at 2.84 MeV). One might be tempted to interpret these excited bands in terms of the conventional concept of the β and γ

bands built on a well-deformed prolate ground state, but, in fact, they are markedly different from them. First, there is a strong mixing of the β- and γ-vibrational components, as seen from strong interband $E2$ transitions between the two excited bands. Second, the calculated ratio of the excitation energies relative to $E(0_2^+)$, $(E(4_2^+) - E(0_2^+))/(E(2_2^+) - E(0_2^+))$, is 2.51, which is far from the rigid-body value. Third, the K-mixing effects are strong, e.g., the $K = 0$ ($K = 2$) components of the 2_2^+ (2_3^+) and 4_2^+ (4_3^+) wave functions are at most 60%. To sum up, although the prolate deformation is appreciably developed in the low-lying states of ^{64}Cr, the large-amplitude shape fluctuations play a dominant role and lead to the strong $\beta - \gamma$ coupling and significant interband $E2$ transitions.

In Fig. 11, we plot the vibrational wave functions at $\gamma = 0.5°$ and the probability density $P(\beta)$ of finding a shape with a specific value of β for the ground and excited 0^+ states in $^{60-64}$Cr. Note that the probability density vanishes at the spherical shape because of the β^4 factor in the volume element. It is seen that, while the ground-state wave function for ^{60}Cr distributes around the spherical shape, those for ^{62}Cr and ^{64}Cr extend from the spherical to deformed regions with $\beta \simeq 0.4$ [see Fig. 11(a)]. Accordingly, the peak of the probability distribution moves toward larger β in going from ^{60}Cr to ^{64}Cr [see Fig. 11(b)]. Concerning the excited 0^+ states, their vibrational wave functions exhibit two peaks: a large peak at the spherical shape and a small peak at a prolate shape [see Fig. 11(c)]. In the probability distribution displayed in Fig. 11(d), the spherical peaks move to the $\beta \approx 0.2$ region and the peaks at $\beta = 0.35$–0.4 in turn become prominent.

The above results indicate that large-amplitude shape fluctuations play an important role both in the ground and excited 0^+ states. The growth of the shape fluctuations leads to an enhancement of the calculated $E0$ transition strengths $\rho^2(E0; 0_2^+ \rightarrow 0_1^+)$ in going from ^{58}Cr to $^{62-66}$Cr, as displayed in Fig. 12.
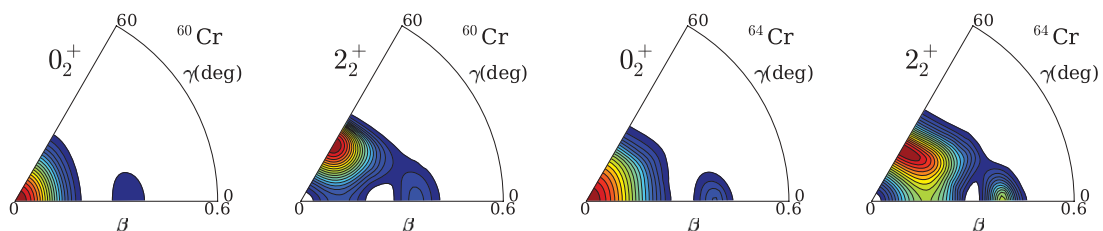

FIG. 10. (Color online) Same as Fig. 6 but for 0_2^+ and 2_2^+ states. The contour lines are drawn at every twentieth part of the maximum value.
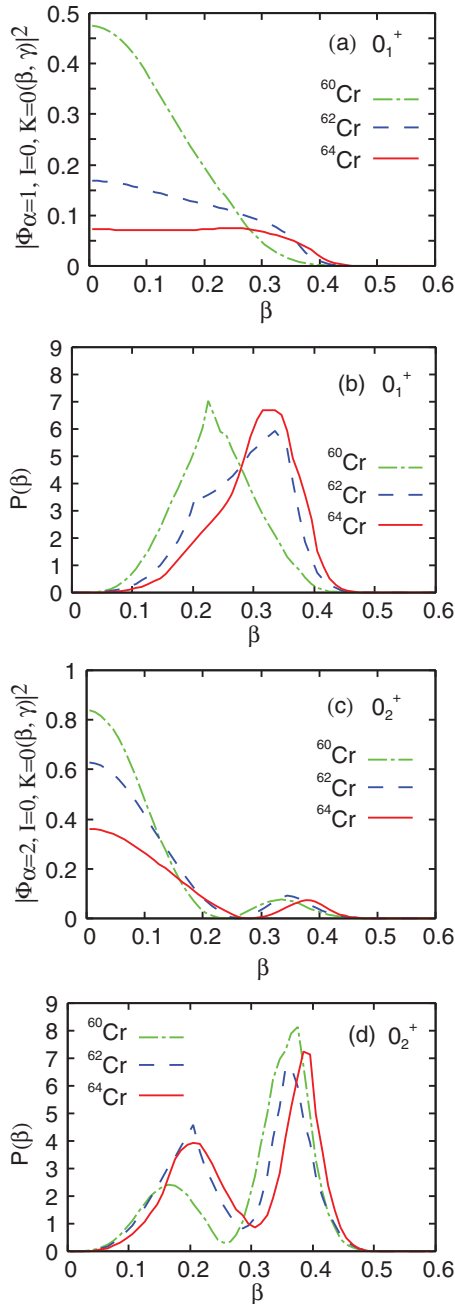
FIG. 12. (Color online) $E0$ transition strengths $\rho^2(E0; 0_2^+ \to 0_1^+)$ calculated for $^{58-66}$Cr.

D. Similarities and differences with the Mg isotopes around $N = 20$

In Ref. [7], Lenzi *et al.* emphasized similarities between the shell structure of the neutron-rich Cr isotopes near $N = 40$ and that of the neutron-rich Mg isotopes around $N = 20$: the neutron $g_{9/2}$ and $d_{5/2}$ single-particle levels above the $N = 40$ subshell play a similar role to the neutron $f_{7/2}$ and $p_{3/2}$ levels above the $N = 20$ shell. The quadrupole matrix elements between these levels are large (because they are spin-nonflip and $\Delta l = 2$). The single-particle levels above and below the $N = 40$ subshell gap ($N = 20$ shell gap) have opposite parities so that the pairing excitations across the gap play an indispensable role to activate the role of the $g_{9/2}$ and $d_{5/2}$ levels ($f_{7/2}$ and $p_{3/2}$ levels) in generating quadrupole collectivity. Also, for protons, the $f_{7/2}$ and $p_{3/2}$ levels in Cr isotopes may play a parallel role to the $d_{5/2}$ and $s_{1/2}$ levels in Mg isotopes.

Indeed, we have found notable similarities between Cr isotopes near $N = 40$ and Mg isotopes around $N = 20$ in our calculation. First of all, the growth of quadrupole collectivity in going from ^{60}Cr to ^{64}Cr is similar to that from ^{30}Mg to ^{32}Mg. In Fig. 6, while the ground state wave function in ^{60}Cr distributes around the spherical shape, they are considerably extended to the prolately deformed region in ^{64}Cr. The 2_1^+ wave function has a peak on the prolate side in ^{60}Cr and it shifts to larger β in ^{64}Cr. These features are similar to those seen in going from ^{30}Mg to ^{32}Mg in our calculation [21]. Concerning the excited 0_2^+ states in ^{60}Cr and ^{64}Cr, as shown in Figs. 11(c) and 11(d), both vibrational wave functions exhibit a two-hump structure. Similar two-hump structures of the excited 0^+ states have been obtained also in our calculation for ^{30}Mg and ^{32}Mg.

On the other hand, we have also found significant differences between the ^{64}Cr region and the ^{32}Mg region. First of all, the K mixing is strong in the excited bands in the Cr isotopes, whereas they are weak in the Mg region. The shape fluctuations toward the γ direction and the effect of the $\beta - \gamma$ coupling are larger in the Cr isotopes than in Mg. This can be clearly seen, for instance, in the 2_2^+ wave functions displayed in Figs. 9 and 10. Lenzi *et al.* [7] found significant mixture of n-particle–n-hole excitations ($n =2,4$ and 6) to the wave functions of Cr isotopes in their shell model calculation. This is consistent with the strong K-mixing found in our calculation.

FIG. 11. (Color online) (a) Vibrational wave function squared $|\Phi_{\alpha=1,I=0,K=0}(\beta, \gamma = 0.5°)|^2$ of the ground states in $^{60-64}$Cr. (b) Probability densities integrated over γ, $P(\beta) = \int d\gamma |\Phi_{\alpha=1,I=0,K=0}(\beta, \gamma)|^2 |G(\beta, \gamma)|^{1/2}$. (c) Same as (a) but for the 0_2^+ states. (d) Same as (b) but for the 0_2^+ states.

In Ref. [9], Gaudefroy *et al.* studied the collective structure in the $N = 40$ isotones and obtained the low-lying states with a vibrational character for ^{64}Cr. Our calculated results indicates that ^{64}Cr is rather deformed but still has a transitional character.
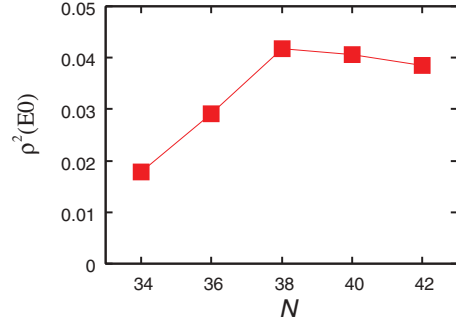
IV. CONCLUSIONS

In this paper, we have investigated the nature of the quadrupole collectivity in the low-lying states of neutron-rich Cr isotopes $^{58-66}$Cr by solving the 5D collective Schrödinger equation. The vibrational and rotational inertial functions and the collective potential in the 5D quadrupole collective Hamiltonian are microscopically derived with use of the CHFB + LQRPA method. The calculated inertial functions include the contributions from the time-odd components of the moving mean field. The results of calculation are in good agreement with the available experimental data. The prolate deformation remarkably develops along the isotopic chain from $N = 36$ to 40. It is not appropriate, however, to characterize the low-lying state of Cr isotopes around ^{64}Cr in terms of the prolate rigid-rotor model: the excitation spectra are still transitional and the large-amplitude shape fluctuations dominate in their low-lying states. The calculated excited bands exhibit strong couplings between the β and γ vibrational degrees of freedom. For close examination of the nature of quadrupole collectivity in these nuclei, experimental exploration of their excited bands is strongly desired.

[1] O. Sorlin *et al.*, Eur. Phys. J. A **16**, 55 (2003).
[2] A. Bürger *et al.*, Phys. Lett. B **622**, 29 (2005).
[3] S. Zhu *et al.*, Phys. Rev. C **74**, 064315 (2006).
[4] N. Aoi *et al.*, Nucl. Phys. A **805**, 400c (2008).
[5] N. Aoi *et al.*, Phys. Rev. Lett. **102**, 012502 (2009).
[6] A. Gade *et al.*, Phys. Rev. C **81**, 051304(R) (2010).
[7] S. M. Lenzi, F. Nowacki, A. Poves, and K. Sieja, Phys. Rev. C **82**, 054301 (2010).
[8] H. Oba and M. Matsuo, Prog. Theor. Phys. **120**, 143 (2008).
[9] L. Gaudefroy, A. Obertelli, S. Péru, N. Pillet, S. Hilaire, J.-P. Delaroche, M. Girod, and J. Libert, Phys. Rev. C **80**, 064313 (2009).
[10] K. Kaneko, Y. Sun, M. Hasegawa, and T. Mizusaki, Phys. Rec. C **78**, 064312 (2008).
[11] Y. Yang, Y. Sun, K. Kaneko, and M. Hasegawa, Phys. Rec. C **82**, 031304(R) (2010).
[12] M. Baranger and K. Kumar, Nucl. Phys. A **110**, 490 (1968).
[13] K. Kumar and M. Baranger, Nucl. Phys. A **110**, 529 (1968).
[14] N. Hinohara, T. Nakatsukasa, M. Matsuo, and K. Matsuyanagi, Prog. Theor. Phys. **119**, 59 (2008).
[15] N. Hinohara, T. Nakatsukasa, M. Matsuo, and K. Matsuyanagi, Phys. Rev. C **80**, 014305 (2009).
[16] N. Hinohara, K. Sato, T. Nakatsukasa, M. Matsuo, and K. Matsuyanagi, Phys. Rev. C **82**, 064313 (2010).
[17] M. Matsuo, T. Nakatsukasa, and K. Matsuyanagi, Prog. Theor. Phys. **103**, 959 (2000).
[18] N. Hinohara, T. Nakatsukasa, M. Matsuo, and K. Matsuyanagi, Prog. Theor. Phys. **117**, 451 (2007).
[19] K. Sato and N. Hinohara, Nucl. Phys. A **849**, 53 (2011).
[20] H. Watanabe *et al.*, Phys. Lett. B **704**, 270 (2011).
[21] N. Hinohara, K. Sato, K. Yoshida, T. Nakatsukasa, M. Matsuo, and K. Matsuyanagi, Phys. Rev. C **84**, 061302 (2011).
[22] K. Yoshida and N. Hinohara, Phys. Rev. C **83**, 061302(R) (2011).
[23] K. Kumar and M. Baranger, Nucl. Phys. A **92**, 608 (1967).
[24] D. J. Thouless and J. G. Valatin, Nucl. Phys. **31**, 211 (1962).
[25] M. V. Stoitsov, J. Dobaczewski, W. Nazarewicz, and P. Ring, Comp. Phys. Comm. **167**, 43 (2005).
[26] National Nuclear Data Center, Brookhaven National Laboratory, http://www.nndc.bnl.gov/.
[27] H. Sakamoto and T. Kishimoto, Phys. Lett. B **245**, 321 (1990).
[28] W. Rother *et al.*, Phys. Rev. Lett. **106**, 022502 (2011).